

JGR Solid Earth

RESEARCH ARTICLE

10.1029/2020JB020713

Key Points:

- Separation of present-day mass transport and glacier isostatic adjustment signatures using multiple observation types
- Estimation of geocenter motion due to past and present-day surface mass changes
- Enhanced glacial isostatic adjustment signals detected in areas of low upper mantle viscosity and recent ice loss

Correspondence to:








Y. Jiang,
yan.jiang@canada.ca

Citation:

Jiang, Y., Wu, X., van den Broeke, M. R., Munneke, P. K., Simonsen, S. B., van der Wal, W., & Vermeersen, B. L. (2021). Assessing global present-day surface mass transport and glacial isostatic adjustment from inversion of geodetic observations. *Journal of Geophysical Research: Solid Earth*, 126, e2020JB020713. <https://doi.org/10.1029/2020JB020713>

Received 2 AUG 2020
Accepted 16 APR 2021

Assessing Global Present-Day Surface Mass Transport and Glacial Isostatic Adjustment From Inversion of Geodetic Observations

Yan Jiang^{1,2} , Xiaoping Wu³ , Michiel R. van den Broeke⁴ ,
Peter Kuipers Munneke⁴ , Sebastian B. Simonsen⁵ , Wouter van der Wal⁶ , and
Bert L. Vermeersen^{6,7} 

¹Natural Resources Canada, Geological Survey of Canada, Sidney, Canada, ²School of Earth and Ocean Science, University of Victoria, Victoria, Canada, ³Jet Propulsion Laboratory, California Institute of Technology, Pasadena, CA, USA, ⁴Institute for Marine and Atmospheric Research, Utrecht University, Utrecht, The Netherlands, ⁵DTU Space—National Space Institute, Technical University of Denmark, Lyngby, Denmark, ⁶Faculty of Aerospace Engineering and Faculty of Civil Engineering and Geosciences, Delft University of Technology, Delft, The Netherlands, ⁷Department of Estuarine and Delta Systems EDS, NIOZ Royal Netherlands Institute for Sea Research, Yerseke, The Netherlands

Abstract Long-term monitoring of global mass transport within the Earth system improves our ability to mitigate natural hazards and better understand their relations to climate change. Satellite gravity is widely used to monitor surface mass variations for its unprecedented spatial and temporal coverage. However, the gravity data contain signals from visco-elastic deformation in response to past ice sheet melting, preventing us from extracting signals of present-day surface mass trend (PDMT) directly. Here we present a global inversion scheme that separates PDMT and visco-elastic glacial isostatic adjustment (GIA) signatures by combining satellite gravimetry with satellite altimetry and ground observations. Our inversion provides global dual data coverage that enables a robust separation of PDMT and GIA spherical harmonic coefficients. It has the advantage of providing estimates of Earth's long wavelength deformation signatures and their uncertainties. Our GIA result, along with its uncertainty estimates, can be used in future GRACE processing to better assess the impact of GIA on surface mass change. Our GIA estimates include a rapid GIA uplift in the Southeast Alaska and the Amundsen Sea Embayment, due to the visco-elastic response to recent glacial unloading. We estimate the average surface mass change rate from 2002–2010 to be $-203 \pm 3 \text{ GT}\cdot\text{a}^{-1}$ in Greenland, $-126 \pm 18 \text{ GT}\cdot\text{a}^{-1}$ in Antarctica and, $-62 \pm 5 \text{ GT}\cdot\text{a}^{-1}$ in Alaska. The GIA low degree spherical harmonic coefficients are sensitive to rheological properties in Earth's deep interior. Our low-degree GIA estimates include geocenter motion and \dot{J}_2 which provide unique constraints to understand Earth's lower mantle and ice history.

Plain Language Summary Surface mass exchange between Earth's "spheres"—atmosphere, hydrosphere, cryosphere, biosphere, and pedosphere—are enormous. Monitoring surface mass change helps to understand climate change and mitigate hazardous effects such as extreme drought or flooding. Measurements of surface mass change are perturbed by subsurface processes, such as mantle flow underneath Earth's crust. Often, a model is used to correct the subsurface signals from observations, and likely to introduce un-modeled process errors into the surface mass estimates. We use a mostly data-driven method to extract present-day surface mass change trends along with their error estimates. The results give an enhanced view of the surface mass processes and can help improving the accuracy of future surface mass estimations. Moreover, we get a more accurate picture of the subsurface processes, that are mainly caused by Earth's viscous response to past ice sheet melting. We find that Earth's crust bounces back more rapidly after glacier melting events than we assumed before, especially in places where the mantle viscosity is low.

1. Introduction

Global climate change modifies the mass redistribution process within Earth system. Present-day surface mass transport, in turn, changes the geoid and global sea level. Surface mass transport, mainly from fluid water moving between Earth's "spheres" impacts societies and its relation to climate change needs to be better understood. Global monitoring of present-day surface mass trend (PDMT), thus, is vital in itself and to

understand climate change. Before the Gravity Recovery and Climate Experiment (GRACE) satellites were launched, large-scale components of mass movement within Earth system were inferred from satellite laser ranging (SLR) observations (Cheng et al., 2013; Cox & Chao, 2002; Dickey et al., 2002). The time-varying gravity field has been monitored continuously with unprecedented accuracy since the GRACE era (Tapley et al., 2004; Wouters et al., 2014). However, GRACE is not only sensitive to PDMT, but also to subsurface mass changes mainly caused by Earth's viscous response to the removal of ice sheets, known as glacial isostatic adjustment (GIA) (Peltier, 2004; Wouters et al., 2014). Although efforts have been made recently to improve our capability to monitor surface mass transport, the current method is still subject to GIA model errors. The presence of the residual GIA signals, specifically GIA signals due to the recent past ice loss, in most geodetic data and unquantified GIA model errors make the direct observation of surface mass transport trend a difficult endeavor.

Present-day surface mass redistribution can be estimated by measuring the instantaneous elastic response of Earth's crust to surface loading changes (Farrell, 1972; Wahr et al., 1998). In practice, the GIA process complicates the interpretation of the linear trend observations. Physical models have been developed to reconstruct present-day GIA signals (Ivins et al., 2013; Peltier et al., 2015, 2018), but such models are largely based on forward-fitting approaches, partial-domain viscosity inversions, piecewise subsequent iterative modifications with new data, and are, thus, subject to ambiguities and uncertainties in the past ice history, Earth rheology, and flow constitutive laws. Consequently, such development processes make the quantification of model uncertainties particularly hard (Caron et al., 2018; van der Wal et al., 2015), although for some cases such as in North America, uncertainty estimates due to lateral viscosity have been presented (Li et al., 2020). Furthermore, ice loading histories in global models generally do not include ice changes in the last centuries in regions of low viscosity such as Antarctica, Alaska, Patagonia, Iceland (Jacob et al., 2012). Thus, mass change estimates in those regions will be biased when global models are used for the correct GIA signal. On the other hand, GIA models with parameters that are fit to regional GIA observations in areas of low viscosity such as in West Antarctica (e.g., Nield et al., 2014) do not capture the low degree signal, while the far-field GIA signal can contribute 40% of the total Antarctic signal (Caron & Ivins, 2020).

Earlier studies suggest that PDMT- and GIA-induced elastic and viscoelastic signatures have distinct spatial-temporal patterns in different observation types (Wahr et al., 1995; Wu et al., 2010). In light of this, regional inversion models that combine multi-type observations have been developed to separate PDMT and GIA (Gunter et al., 2014; Martín-Español et al., 2016; Sasgen et al., 2017; Simon et al., 2017). These regional inversions solve GIA and PDMT simultaneously, and are successful in providing mass transport information on a local scale. However, they cannot assess the impact of geocenter motion, nor deliver global long-wavelength spherical harmonic coefficients. On the other hand, global inversion of GIA and PDMT is difficult due to the paucity of dual observation types in both the oceans and the interior of the Greenland and Antarctic ice sheets.

Here, for the first time, we develop a high-resolution method to combine data from multiple observation platforms to assure global coverage of dual observation types in estimating PDMT and GIA simultaneously. Our results provide nearly data-driven estimates of PDMT, including global non-steric sea level change, and valuable spherical harmonic coefficient constraints on ice history and lower mantle viscosity. Compared to global dynamic GIA models, coefficient ambiguities and uncertainties are reduced by our use of precise global geodetic data, and the effect of recent ice unloading is included. Our estimates also include long-wavelength signal that is missing in regional inversions (empirical GIA estimates). GRACE and GNSS have been used to measure precisely the load induced deformation at both local and global scales (Blewitt et al., 2001; Wahr et al., 1998; Wu et al., 2010). Although both data sets have the potential to reach global coverage, for our inversion needs, gaps in both spatial and temporal domains exist. The following are a few examples: the GRACE data system is not sensitive to degree-1 geocenter motion; GNSS station distribution is sparse over the ocean and near glaciers; GNSS data gaps and discontinuities exist in the time series; crustal deformation signals from tectonics also complicate the interpretation. For our purpose of separating global PDMT and GIA, it is vital to use complementary data for global dual coverage and reconcile information from overlapping observations to reduce uncertainties. We, therefore, present a kinematic inversion that takes advantage of the multiple globally distributed data sets to separate PDMT and GIA with a robust uncertainty estimation. In addition to GRACE observations, we included 786 geodetic stations on land to

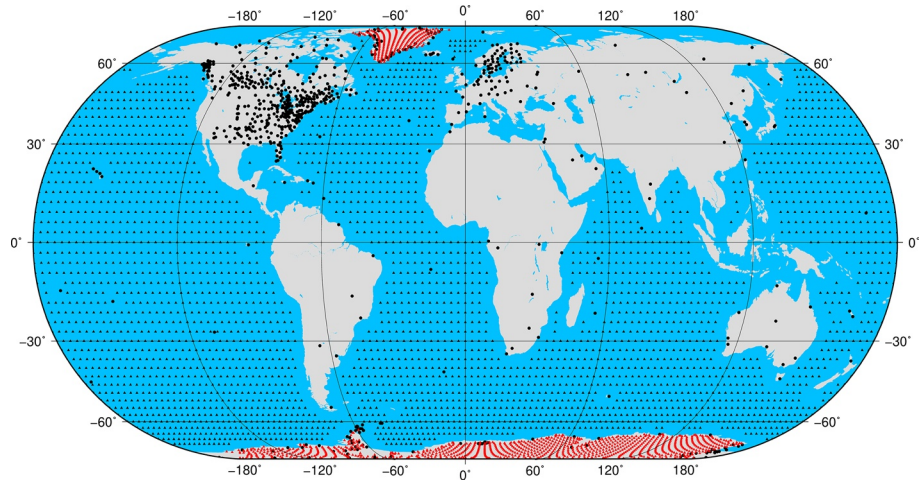


Figure 1. Distribution of global data sets. We use surface geodetic station velocities (black dots, GNSS/VLBI/SLR), ocean bottom pressure from the ECCO model (black triangles), ICESat (red dots) elevation change rate over the Greenland and Antarctic ice sheets, and GRACE spherical harmonic coefficients (not shown here). All data are sampled from 2002 to 2010. ECCO, Estimating the Circulation and Climate of the Ocean; GRACE, Gravity Recovery and Climate Experiment; SLR, satellite laser ranging.

help separate GIA and PDMT (Figure 1). Ocean bottom pressure (OBP) results from JPL's Estimating the Circulation and Climate of the Ocean (ECCO) model (<https://ecco.jpl.nasa.gov/products/all/>) were included to help separate GIA and PDMT in the ocean (Fukumori et al., 1999). Previous work by Wu et al. (2010) suffered from a lack of dual observation types in the interior of the Greenland and Antarctic ice sheets, resulting in considerable GIA uncertainties in these two regions. Here, we supply new ICESat elevation change rates over these ice sheets to fill the data gaps (Figure 2) that arose in Wu et al. (2010).

In this study, we present a simultaneous PDMT and GIA estimation using the method mainly developed in Wu et al. (2010), but with a much improved globally distributed observation network of multiple satellite and ground data, including ICESat altimetry in particular, and improved resolution and accuracy from a number of observation techniques. We first describe the three data types and the OBP model as well as their processing strategies in detail in Section 2. We conduct the inversion in the spectral domain from degree 1 to 60 for the GIA signatures and up to degree 180 for the PDMT. The inverse methodology is presented with detail in Section 3. Our inverted results for both GIA and PDMT in spherical harmonic and spatial domains are presented in Section 4, followed by discussion and conclusions in Section 5.

2. Observation Types and Data Processing Methods

GIA-induced deformation and gravity changes have long relaxation times and, thus, are reasonable to be approximated by linear rates over the time scale of our study, except for a few areas of low viscosity where relaxation time can be in the order of decades such as parts of the Antarctica (e.g., Nield et al., 2014). On the other hand, PDMT has considerable annual and inter-annual variability, and is accelerating in the Polar Regions and certain glaciated mountain regions (Harig & Simons, 2015; Jiang et al., 2010; Scambos et al., 2004; Shepherd et al., 2018, 2020). To minimize the effect of nonlinear PDMT variations in different data sets, and to maximize the overlapping time from multiple observations, we choose to pre-process all the data to derive linear change rates from the period of 2002–2010 which is the only time window when all four data sets are available. Longer data sets exist for GRACE, OBP, and GPS, but not for ICESat, and the PDMT rate has changed considerably since 2010 (Shepherd et al., 2018).

We use CSR RL06 GRACE monthly solutions with spherical harmonics degree and order 60. GRACE C_{20} coefficient time series are replaced with estimates from SLR (Cheng et al., 2013). The GRACE data system is insensitive to geocenter motion, which is driven by degree-one mass changes of both PDMT and GIA. We do not correct the PDMT and GIA degree-one coefficients, but estimate them in the subsequent global inversion. Calibrated full covariance matrices up to a degree and order 60 (John Ries, private communication)

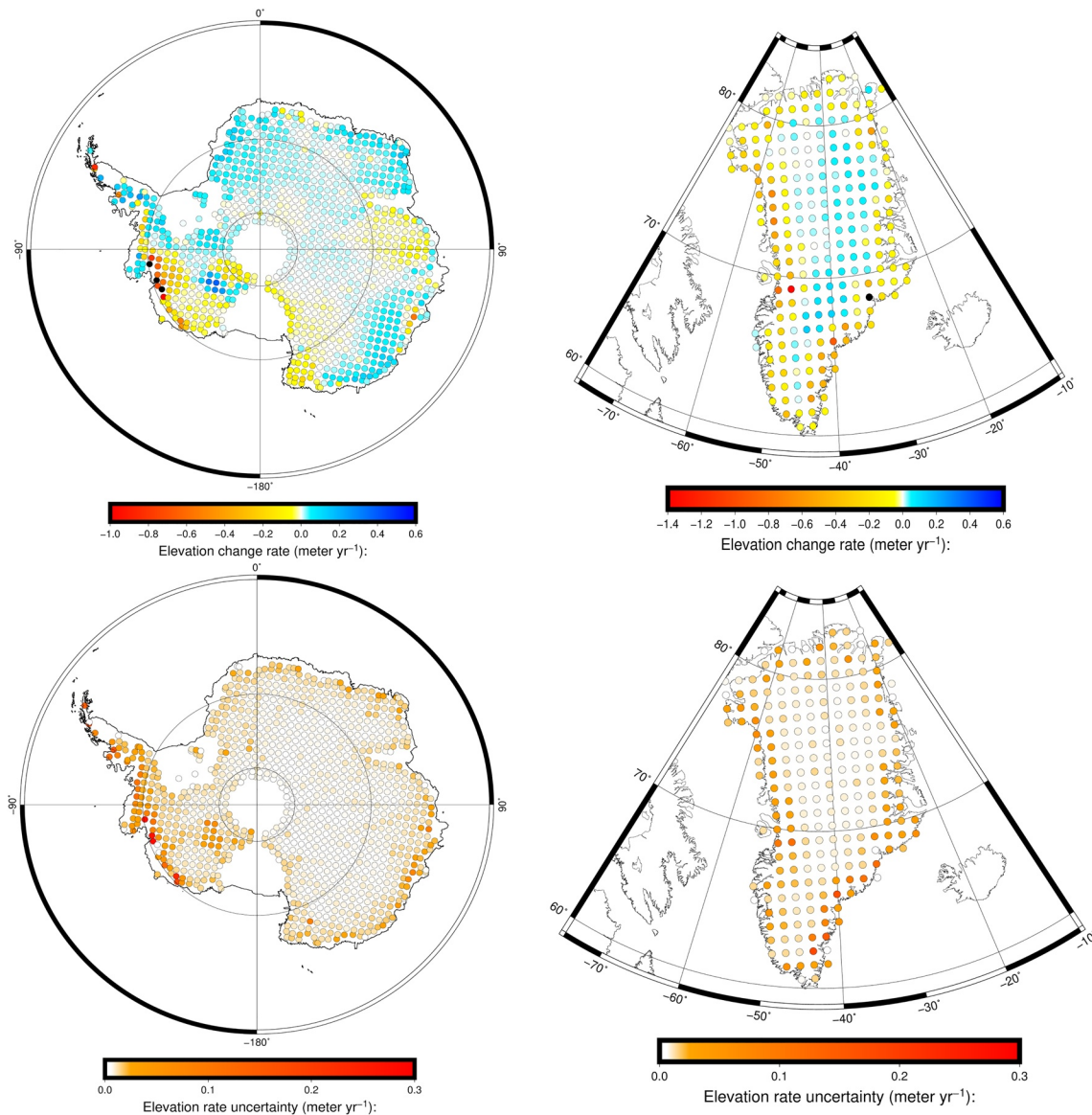


Figure 2. (Left) Enlarged map of Antarctica ICESat elevation change rate and uncertainty. We have excluded ICESat data over floating ice shelves. Each colored dot represents a 100 by 100 km grid box on the ice sheet. The average vertical rates within that grid box are color-coded. The rate uncertainty defined as 2-sigma confidence values of the residual elevation rates after subtracting the mean rate of the 100 by 100 km grid. The ICESat elevation rate uncertainty reflects not only the noise character of ICESat data itself, but also changes in ice surface topography, and heterogeneity in ice dynamics within the grid. We find that data uncertainties on the periphery of the ice sheet are 2–3 times larger than in the interior, reflecting a smoother topography and less change in ice dynamic behaviors in the interior of the ice sheet. Note the difference in color scale for the Antarctica and Greenland plot. (Right) Enlarged map of Greenland ICESat elevation change rate and uncertainty.

are used in deriving the trends and their full covariance matrix. in order to reduce regional tectonic effects, we fit and remove the spherical harmonic co-seismic deformation patterns of the 2004 Sumatra Earthquake and the 2007 Southern Sumatra Earthquake near Bengkulu from GRACE coefficient rates (Han et al., 2013).

We use monthly ECCO-JPL OBP products (Fukumori et al., 1999) to derive linear trends in $3^\circ \times 3^\circ$ grid cells. The assimilated OBP results provide oceanographically induced surface load information, and do not account for tectonic and non-tectonic signals, such as earthquake, and GIA induced deformation. In the inversion, the OBP trends are modeled as mass changes within the water column between the sea surface and the time-variable geoid due to dynamic ocean circulation. However, the OBP products are not actual measurements and contain random and spatially correlated errors. Although Wu et al. (2010) included a

large random error component in their diagonal covariance matrix, spatial correlation was neglected. Such an approach significantly simplified and underestimated the true errors in the OBP trends, especially in the long-wavelength domain. To mitigate this problem, we add a spatially correlated error component to the covariance matrix of the OBP trends to allow for likely long-wavelength errors. We add a 500-km Gaussian correlated error component in the construction of the covariance matrix for the OBP trends. The amplitudes of the random and correlated components are chosen to be consistent with the grid point differences and low-degree spherical harmonic differences of two OBP models (ECCO and the Ocean Model for Circulation and Tides [Dobslaw & Thomas, 2007]). Such an empirical covariance matrix will serve to strengthen the error statistics of the global inversion.

We choose space-geodetic stations in tectonically stable regions that have more than three years of data to calculate the long-term crustal motion rate. To increase spatial resolution in areas of rapid mass changes, we densify the station coverage by adding regional GPS networks in Greenland, SE Alaska, and Antarctica. We only use vertical results for the sites located in SE Alaska to avoid possible bias in horizontal velocities from regional tectonics. We include additional stations that are installed after 2010, but near GIA deformation centers (e.g., Hudson Bay, Canada), and whose time series are only exhibiting linear motion. We process daily GPS data in five-minute batches with JPL's GIPSY 6.4 software. We estimate wet tropospheric delay and receiver clocks together with station coordinates. The Vienna Mapping Function (Boehm et al., 2006) is used to map zenith tropospheric delay to lower-elevation angles. We use the FES2004 ocean tide model (Lyard et al., 2006) to correct the surface displacements caused by ocean tides. JPL's non-fiducial orbits are used for data reduction, and then we align all station coordinates to the IGB08 reference frame (Reischung et al., 2012). Finally, station velocities in the east, north, and up directions are derived separately (Jiang et al., 2012), and are further projected to remove the ITRF network translation information to avoid contamination from a possible origin drift of the reference frame (Wu et al., 2010).

NASA's ICESat mission measures long-term surface elevation changes in the Polar Regions (Schutz et al., 2005; Zwally et al., 2002). In this study, we use ICESat data in Greenland and Antarctica from 2003.0-2010.0 to provide additional information on present-day ice mass change. We process both ICESat RL633 and RL634 data in a consistent way, but report only results from the RL 634 data set. The major differences are that the RL634 data have been corrected for the Gaussian Centroid (G-C) error (Borsa et al., 2014), which will have impacts on the ICESat inter-campaign bias (ICB). The ICB has been estimated to be in the range of 1–2 cm·a⁻¹ (Scambos & Shuman, 2016; Zwally et al., 2015). In our inversion, we do not correct for ICB from the raw ICESat observations, but estimate the inter-campaign bias trend as an additional parameter in the inversion. We assume that the ICB trend is constant in both Greenland and Antarctica, and estimate one auxiliary ICB trend parameter to mitigate possible biases introduced by ICESat. We first perform data reduction based on a set of quality flags indicating the health of the space segment, signal quality, saturation level, return surface character, and cloud cover. Then we use along-track ground repeat track data from early 2003 to the end of 2009 to calculate surface elevation changes accounting for topography, slope, and elevation at each 1 km by 1 km grid cell. We convert the volumetric change to ice mass change using estimates from regional climate models. In Greenland, the ICESat derived elevation rate is first corrected for firn compaction rate (Sørensen et al., 2011) using results derived from a regional climate model HIRHAM5 RCM (Lucas-Picher et al., 2012; Simonsen et al., 2013) within each grid cell. Then the corrected volumetric change is converted to a mass change rate using density values derived from the HIRHAM5. We use a simple glaciological criterion to determine the density in each grid box. We assume that the volume change is caused purely by ice dynamics when the grid cell is located below the equilibrium line (at which the surface mass balance is zero), and an ice density of 917 kg/m³ is used for conversion. When the grid cell is located above the equilibrium line, a composite density that represents the average density for all layers in the vertical column is used during the conversion. In Antarctica, the volume to mass conversion is based on the regional atmosphere and climate model RACMO2.3p2 (van Wessem et al., 2018). We first determine a firn compaction rate and its uncertainty for the period of ICESat operation from the firn densification model (FDM). The FDM calculates time-varying firn depth and density variations by accounting for the information on firn processes such as melt percolation and refreezing air content. We correct the ICESat elevation rate using the firn compaction velocity. The elevation rate uncertainty includes both the standard deviation of ICESat and the formal error of the firn correction. The residual elevation rate is considered the result of elevation change due to ice dynamics only. In converting volumetric change to mass change for the

ice layer, we use ice density for the entire Antarctic ice sheet except where large positive residuals are found. When the positive residual values are larger than the 95% confidence level, we attribute the residual uplift to un-modeled snow accumulation, and an average firn density is used. We then add the surface mass balance from the firn layer in the RACMO2.3p2 model to derive the total mass change rate. The volume-to-mass conversion in Antarctica differs from Greenland in that we assume that the firn compaction corrected ICE-Sat elevation rates are due to ice dynamics only and mass balance in the firn layer is derived from the RACMO2.3p2 model output. Lastly, we average ICESat results in both Greenland and Antarctica into 100 km by 100 km grid boxes for them to be consistent with the spatial resolution of our global inversion (Figure 2).

3. Global Kinematic Inversion Methodology

Our inversion separates PDMT and GIA signatures in the spectral domain using information from multiple data sets. GRACE measures geoid change rates due to both PDMT and GIA with near global coverage. Surface geodetic stations measure the sum of elastic and viscous crustal deformation rates in response to current and past mass redistribution. ICESat data are sensitive to current ice and firn volume changes and total bedrock uplift due to both elastic and viscous deformation in the polar regions. OBP products complement these data sets by providing partial PDMT constraints in the ocean basins.

3.1. Measurement Models

The observation equations for ground geodetic velocities, GRACE geoid coefficient rates, and OBP rates were described in the supplementary material of Wu et al. (2010). These are listed and briefly reviewed here for reference and ease of discussion, along with the new observation equation for ICESat altimetry data. Throughout this paper, we will use a coordinate system with its origin defined at the center-of-mass of solid Earth (CE) with consistent load Love numbers. In this system, the ground station velocities at (θ, φ) relative to the center-of-mass of the total Earth system (CM) can be written as follows:

$$\dot{r} - \dot{r}_{cm} = \omega_p \times r + \frac{4\pi a^3}{M_E} \sum_{n=1}^{\infty} \sum_{m=0}^n \sum_{q=c,s} \frac{1}{2n+1} \times \left[\left(\dot{h}'_n \dot{M}_{nmq} + \dot{M}_{nmq}^{v,h} \right) Y_{nmq} \hat{e}_r + \left(\dot{l}'_n \dot{M}_{nmq} + \dot{M}_{nmq}^{v,l} \right) \left(\partial_\varphi Y_{nmq} \hat{e}_\varphi + \frac{1}{\sin \vartheta} \partial_\varphi \partial_\vartheta Y_{nmq} \hat{e}_\varphi \right) \right] - \dot{r}_{cm}, \quad (1)$$

where the vectors \dot{r} and \dot{r}_{cm} are the station velocity and the velocity of CM in our coordinate system respectively. ω_p is the angular velocity of the p th plate, $p = 1, \dots, 15$ including major tectonic plates with at least 3 surface geodetic sites. a and M_E are the radius and mass of the Earth, respectively. Y_{nmq} is the real normalized spherical harmonic function (with geodetic convention) of degree n and order m , with $q = c, s$ indicates the cosine or sine term. Note that there is no sine term if $m = 0$. h'_n and l'_n are vertical and horizontal elastic load Love numbers, respectively. \dot{M}_{nmq} are the spherical harmonic coefficients of present-day surface mass density trend (a typical form of PDMT) in units of $\text{kg m}^{-2} \text{a}^{-1}$. $\dot{M}_{nmq}^{v,h}$ and $\dot{M}_{nmq}^{v,l}$ are spherical harmonic coefficients of GIA induced surface vertical and horizontal velocities, respectively, expressed in units of apparent surface mass density rate, and describe kinematic GIA signatures in ground geodetic data. \hat{e}_r , and the like indicate unit spherical coordinate vectors.

Nominally, the velocity of CM relative to CE (our coordinate origin) has two components, $\dot{r}_{cm} = \dot{r}_{cm}^e + \dot{r}_{cm}^v$ where the superscript e and v indicate the PDMT and GIA contributions, respectively. GIA does not cause current variations of water mass in the surface layer other than its passive response to the changing gravity potential due to GIA. This passive response is included as a part of PDMT in our study. Therefore, $\dot{r}_{cm}^v = 0$. Consequently, geocenter motion between CM and the center-of-figure of the solid Earth surface (CF) can be expressed as follows:

$$V_G = \dot{r}_{cm}^e - \dot{r}_{cf}^e - \dot{r}_{cf}^v = \frac{4\pi a^3}{\sqrt{3}M_E} \times \left[\left(\dot{M}_{11c} - \frac{\dot{M}_{11c}^h + 2\dot{M}_{11c}^l}{3} \right) \hat{e}_x + \left(\dot{M}_{11s} - \frac{\dot{M}_{11s}^h + 2\dot{M}_{11s}^l}{3} \right) \hat{e}_y + \left(\dot{M}_{10c} - \frac{\dot{M}_{10c}^h + 2\dot{M}_{10c}^l}{3} \right) \hat{e}_z \right], \quad (2)$$

where $\dot{M}_{lmq}^h = h_1' \dot{M}_{lmq} + \dot{M}_{lmq}^{v,h}$, and $\dot{M}_{lmq}^l = l_1' \dot{M}_{lmq} + \dot{M}_{lmq}^{v,l}$. The first term for each coordinate component on the right-hand side of Equation 2 is in fact the component for $\dot{r}_{cm}^e = \dot{r}_{cm}^e$, which should be substituted into Equation 1. The terms containing elastic load Love numbers (not including the negative sign) are the components for $\dot{r}_{cf}^e \cdot \dot{r}_{cm}^e - \dot{r}_{cf}^e$ is, thus, the PDMT contribution to geocenter motion. The remaining terms indicated by superscript v are the visco-elastic components for \dot{r}_{cf}^v , and $\dot{r}_{cm}^v - \dot{r}_{cf}^v = -\dot{r}_{cf}^v$ is the GIA contribution to geocenter motion.

Similarly, GRACE measured gravitational geoid rate spherical harmonic coefficients can be described by the following equation:

$$\dot{N}_{nmq} = \frac{4\pi a^3}{M_E(2n+1)} \left((1+k_n') \dot{M}_{nmq} + \dot{M}_{nmq}^{v,k} \right), \quad (3)$$

where k_n' is the potential load Love number and $\dot{M}_{nmq}^{v,k}$ is the spherical harmonic coefficients for the GIA-induced geoid change rate expressed in units of apparent surface mass density rate. Here, $n = 2, 3, \dots, 60$ in GRACE's level-2 data release RL-6.

The JPL ECCO OBP product is derived in a closed oceanic system with no water mass input or output. ECCO products use the Boussinesq approximation where the density variations are ignored. As is usually done, we apply a mass conservation correction to the OBP values by removing a uniform layer of excess water mass resulting from the Boussinesq approximation. For such corrected OBP values, it is adequate to model the dynamic OBP as the difference between the total PDMT OBP and its hydrostatic equilibrium part. In other words, the oceanographic OBP is the bottom pressure caused by the water column between the sea surface and the equilibrium (time-varying) gravitational geoid changes due to PDMT. The latter surface change depends only on instantaneous global surface mass distribution and reflects the self-attraction and loading effects on the geoid. Again, the hydrostatic part due to GIA with the present-day water redistribution is considered a part of PDMT here. Thus, the following is true at the oceanic grid points:

$$\dot{P} = g \sum_{n=1}^{\infty} \sum_{m=0}^n \sum_{q=c,s} \dot{M}_{nmq} Y_{nmq} - g \dot{M}_{EQ}, \quad (4)$$

where g is normal gravity on the Earth's surface. \dot{M}_{EQ} is hydrostatic equilibrium surface mass density over the oceans and is a function of \dot{M}_{nmq} only.

The ICESat surface elevation rates are modeled as follows:

$$\dot{h} = \dot{b} + \frac{1}{\rho} \left[\sum_{n=1}^{\infty} \sum_{m=0}^n \sum_{q=c,s} \dot{M}_{nmq} Y_{nmq} - \dot{M}_{atm} \right] + (\dot{r} - \dot{r}_{cm}) \cdot \hat{e}_r, \quad (5)$$

where \dot{b} is a bias drift parameter to accommodate a possible drift error due to inter-campaign biases. ρ is ice or modeled firm density depending on the ground track location. \dot{M}_{atm} is the atmospheric mass change rate per unit surface area computed by the ECMWF Re-Analysis ERA-Interim model. Equation 1 can be substituted into the bedrock uplift rate term (the third term on the right-hand side) so that the observation is completely described by the bias drift, PDMT, and GIA parameters.

3.2. Parameterization and a Priori Information

We parameterize our inverse problem similar to that of Wu et al. (2010), except that PDMT coefficients are estimated up to a higher degree and order to accommodate ICESat's high-resolution data. It is well known that in the approach of spherical harmonic inversion, the truncated higher-degree terms, although small, will alias into the low-degree harmonic estimates along with data noises. The total uncertainty, including the aliasing effect and data noise, can be assessed using a properly constructed data and a priori parameter covariance matrix in a constrained least square method. Here, the truncation degree is chosen in a trial-and-error manner. Benefiting from the dense ICESat vertical velocity estimates in the polar regions, we

extend the PDMT spherical harmonic degree to 180 to account for large spatial variability of the ice mass change. In doing so, we are able to limit the aliasing errors from high-degree PDMT parameters to lower-degree PDMT and GIA parameters.

We use a similar degree and order 60 parameterization for the GIA spherical harmonics, as the GIA related deformation is generally longer-wavelength in nature. These include vertical and horizontal coefficients from $n = 1$ to 60. The geoid GIA coefficients are approximately proportional to the corresponding vertical coefficients (Wahr et al., 1995) as follows:

$$\dot{M}_{nmq}^{v,k} \approx \dot{M}_{nmq}^{v,h} \times \frac{2}{2n+1} \text{ for } n \geq 2 \quad (6)$$

However, this relation contains significant errors at low-degrees and does not account for the rotational feedback effects of the GIA process. We therefore retain $\dot{M}_{nmq}^{v,k}$ for $2 \leq n \leq 7$ as additional unknown GIA parameters, and use the approximate relation above to substitute higher-degree $\dot{M}_{nmq}^{v,k}$ in Equation 3 with vertical coefficients $\dot{M}_{nmq}^{v,h}$ multiplied by the corresponding proportionality constants in Equation 6. As shown in the observation equations, our parameter vector also includes 15×3 plate rotation parameters and a constant altimeter bias drift.

Despite the use of multiple globally distributed data sets, our inverse problem remains a rank deficient and underdetermined problem. For example, the relative velocities used to remove ITRF origin drift are only sensitive to $\dot{M}_{1mq}^{v,h} - \dot{M}_{1mq}^{v,l}$ rather than the individual $n = 1$ GIA coefficients. As another example, ICESat's dense ground tracks require a high spherical harmonic truncation. But away from the ice sheets, high spatial resolution data coverage above GRACE's truncation degree of 60 is generally not available. To overcome these problems, careful assessment and incorporation of a priori information are required. Instead of using mathematically convenient models to stabilize the inversion, we construct our a priori parameter information based on physically plausible Earth models. Since the values of PDMT are barely known before, we set all a priori values of PDMT parameters to 0. The a priori GIA parameter values are computed from the average of global ICE-5G and Antarctic IJ05 (Ivins & James, 2005) ice models based on a simplified VM2 Earth rheology profile. The degree-2 and order 1 GIA coefficients are from Paulson et al. (2007a) that is also based on ICE-5G and VM2 models, but includes a revised rotational feedback mechanism (Mitrovica et al., 2005; Peltier, 2015). The a priori values of plate rotations and ICESat bias drift are all set to 0.

We construct a loose but plausible high-resolution a priori PDMT covariance matrix that stipulates much higher PDMT variability over ice and land areas than over the oceans to accommodate the previously observed large variability in ice mass balance and terrestrial water storage. The covariance matrix also includes both random and correlated components in space. With realistic high-resolution geographic boundaries, this a priori information will strengthen isolation of signal sources and improve spatial resolution. Although the a priori GIA model is fairly close to state-of-the-art, unfortunately, its uncertainties are largely unknown. To account for plausible uncertainties in our kinematic GIA parameters, we construct an a priori covariance matrix by perturbing the GIA model dynamically with large ice history and mantle viscosity variations. We use a simplified layered viscoelastic Earth model based on VM2 with an elastic lithosphere, two viscoelastic mantle layers, and an inviscid fluid core for our calculations and propagate the covariance matrices to the kinematic parameter domain. The horizontal extent of the deglaciation is fixed liberally over possible areas, either confirmed or suspected, in the literature, including Alaska. We use random ice thickness uncertainties that are roughly 75% of the ICE-3G model values (Tushingham & Peltier, 1991). Spatially correlated thickness errors are also assumed with an uncertainty of 750 m and a correlation length of 600 km. For Greenland and Antarctica, we include additional correlated thickness errors with an uncertainty of 1 km and a correlation length of 250 km to reflect the less constrained deglaciation history there. We assume that the a priori upper and lower mantle viscosity values have uncertainties of 4×10^{20} Pa s and 7.8×10^{21} Pa s. The covariance matrices of these errors are propagated to our parameter domain and summed up with an additional small diagonal matrix so that the resulting a priori covariance matrix is full ranked and roughly reflects the differences of various ice history and Earth rheology models. It also includes cross-correlations between low-degree GIA geoid coefficients and vertical coefficients, and other intrinsic information on GIA dynamics. While the ice thickness history and Earth rheology constraints are pretty

loose, the dynamically constructed full a priori GIA covariance matrix provides valuable tight constraints for the remainder linear combinations of the GIA spherical harmonic model coefficients based on physical laws that govern the GIA process, and global horizontal extent of historical deglaciation.

To obtain a meaningful solution of the parameters and their realistic uncertainties, we adopted a least squares estimation method with reduced a priori information. The observation equation in matrix form is as follows:

$$L = HX + \Delta \quad (7)$$

where L is the $l \times 1$ observation vector which includes the projected surface geodetic vertical and horizontal velocity, gridded OBP rate and height change rate of the ICESat, plus the GRACE geoid coefficients. Note that the displacement equations in Equation 7 are the projected version of Equations 1–5. X is the $k \times 1$ parameter vector. Equation 7 is further re-organized as follows to include the a priori parameter vector X_0 by subtracting HX_0 from both sides of Equation 7:

$$\Delta_L = H\Delta_x + \Delta \quad (8)$$

where $\Delta_L = L - HX_0$ and $\Delta_x = X - X_0$. This observation equation can be solved using the classical least squares method with a priori information. Here we adopt the method used in Wu et al. (2010) to improve the solution by using a customized singular value decomposition (SVD) method to compare the data and parameter covariance matrices. The data and a priori parameter covariance matrices C_Δ and C_x are first square root decomposed into the following:

$$C_\Delta = R_\Delta^{-1} R_\Delta^{-T}, \quad (9)$$

$$C_x = R_x^{-1} R_x^{-T}, \quad (10)$$

where R_Δ and R_x are upper triangular square root information matrices. We then multiply Equation 8 by R_Δ

$$R_\Delta \Delta_L = R_\Delta H \Delta_x + R_\Delta \Delta. \quad (11)$$

we re-write Equation 11 in terms of the normalized vectors as follows:

$$y = Bz + \delta, \quad (12)$$

where the normalized data, noise, and parameter vectors are defined as follows:

$$y = R_\Delta \Delta_L, \delta = R_\Delta \Delta, z = R_x \Delta_x,$$

and

$$B = R_\Delta H R_x^{-1}$$

We obtain the solution to Equation 12 using the following singular value decomposition of the new observation matrix:

$$B = U\Lambda V, \quad (13)$$

where U and V are $l \times l$ and $k \times k$ orthogonal matrices, and Λ is the $l \times k$ rectangular diagonal matrix, where the first $k \times k$ diagonal matrix containing the singular values λ_i in descending order. We define the first $k \times k$ diagonal matrix of Λ as

$$\Lambda_k = \begin{pmatrix} \Lambda_1 & 0 \\ 0 & \Lambda_2 \end{pmatrix} \quad (14)$$

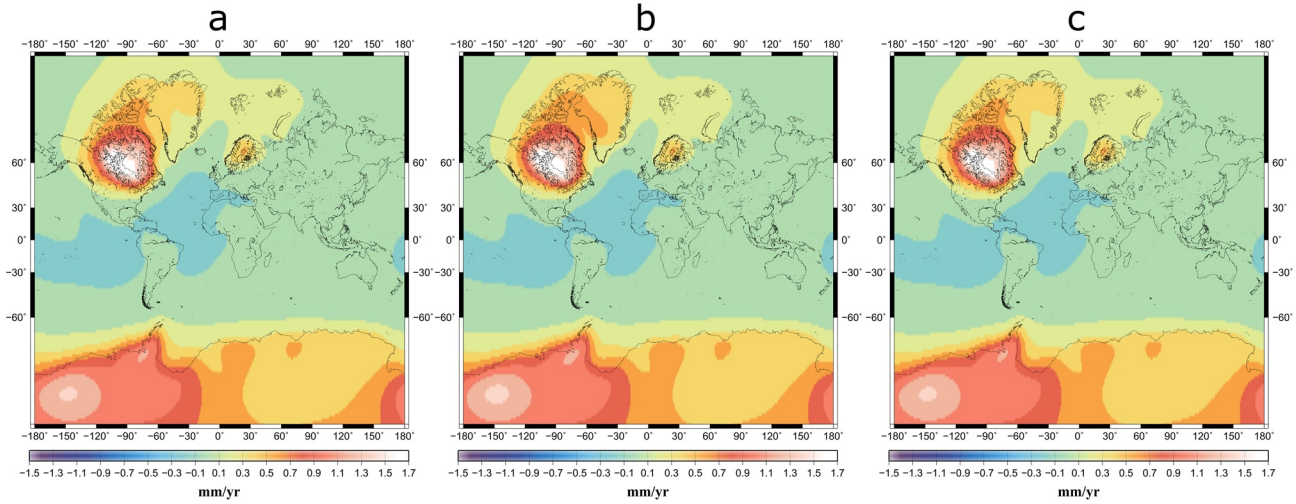


Figure 3. Global simulation results. We have combined an arbitrary global GIA geoid rate truth with PDMT truth. Both GIA and PDMT truth are truncated to spherical harmonic degree and order 60. We then produce synthetic data sets for all surface geodetic sites, ICESat (Greenland only), OBP, and GRACE measurements. We show inversion results with and without ICESat data to highlight the improvements of including ICESat data in Greenland. (a) Input GIA geoid rate truth. (b) Inversion results without including Greenland ICESat data. (c) By including ICESat data in Greenland, we are able to recover GIA signal in Greenland better. The result shows negligible difference in Greenland GIA with the truth data. GIA, glacial isostatic adjustment; OBP, ocean bottom pressure; PDMT, present-day surface mass trend.

A cutoff threshold λ_c is set to separate all singular values into group Λ_1 and Λ_2 , where all values in Λ_1 are greater than λ_c , and Λ_2 includes all singular values less than or equal to λ_c .

We obtain the final solution as follows:

$$\hat{X} = X_0 + R_x^{-1} V^T \Gamma U^T R_\Delta (L - HX_0) \quad (15)$$

where the regulation matrix Γ defined as follows:

$$\Gamma = \begin{pmatrix} \Lambda_1^{-1} & 0 & 0 \\ 0 & (\Lambda_2^2 + I)^{-1} & \Lambda_2 & 0 \end{pmatrix} \quad (16)$$

The key elements in the inversion are the data and a priori parameter covariance matrices and the cutoff threshold λ_c . The cutoff threshold reflects the relative strength of data and a priori information to the solution. It is apparent that, when the singular values are large, the solution does not depend on the a priori model. This avoids unnecessary contamination from possible large model errors. However, the a priori model helps to stabilize the inversion when the singular values are small. The choice of λ_c is done in an ad hoc manner and we use the value of 1 in our study.

To validate our inversion algorithm and demonstrate the improved resolution in the polar regions from added ICESat data, we perform a simulation study using synthetic data with and without ICESat data in Greenland (Figure 3). We generate synthetic surface geodetic/ICESat/OBP/GRACE observations from reference GIA (Figure 3a) and PDMT scenarios as well as MORVEL plate model (DeMets et al., 2010). We also generate data noise according to the data covariance matrices from real observations. To convert PDMT into ICESat elevation change, we use a uniform firn density of 600 kg/m^3 . For simplicity, we include only Greenland ICESat data in the simulation. Adding more ICESat data in Antarctica will not change our conclusion. We compare inversion results with and without ICESat data to show the achieved improvement. In the presence of noise, the inversion without ICESat recovers the truth to within uncertainty (Figure 3b). Nevertheless, when we include the ICESat data, the truth is recovered with better accuracy (Figure 3c).

Table 1
Geocenter Motion and Regional Mass Transportation From Our Joint Global Inversion

	Velocity (mm·a ⁻¹)
GIA geocenter motion (CE w.r.t. CF)	
X	-0.11 ± 0.01
Y	0.13 ± 0.02
Z	-0.72 ± 0.06
PDMT geocenter motion (CM w.r.t. CF)	
X	-0.19 ± 0.07
Y	0.07 ± 0.08
Z	-0.16 ± 0.08
ICESat elevation bias drift	6.03 ± 1.70
Non-steric global sea level	1.37 ± 0.13
^a PDMT induced \dot{J}_2	$(6.0 \pm 0.5) \cdot 10^{-11}$
^a GIA induced \dot{J}_2	$(-3.9 \pm 0.3) \cdot 10^{-11}$
	Mass change rate (GT·a ⁻¹)
Alaska	-62.4 ± 4.8
Antarctica: Total	-126.4 ± 18.4
West Antarctica	-111.8 ± 4.0
East Antarctica	5.6 ± 16.7
Antarctica Peninsula	-20.3 ± 2.2
Greenland	-203.3 ± 3.1
CAA	-49.4 ± 5.6
Arctic Ocean	-1.5 ± 8.7

Abbreviations: CAA, Canadian Arctic Archipelago; GIA, glacial isostatic adjustment; PDMT, present-day surface mass trend.

^aUnit for \dot{J}_2 is a⁻¹.

ICESat derived mass change rates depend on the average density profile used for the firn layer. As presented in the above section, the density profile is determined from ICESat residual values after the firn compaction correction. The ICESat residual velocity is a function of GIA and PDMT induced vertical velocities. Thus, our method requires iteration to update the firn density. We first compute the surface uplift from our initial GIA and PDMT values, then we iterate our inversion to update the firn density profile. Our inversion commonly converges within 1–2 iterations, indicating small GIA and PDMT vertical rates compared to ICESat elevation rates.

4. Inversion Results

Table 1 summarizes the key parameters in our inversion. Our PDMT results show strong mass loss in Greenland and West Antarctica, up to 10 cm·a⁻¹ water equivalent mass change (Figure 4). The average total mass loss rate from 2002–2010 is 126.4 ± 18.4 GT·a⁻¹ for Antarctica and 203.3 ± 3.1 GT·a⁻¹ for Greenland. Our Greenland mass loss estimate is significantly larger than that of Wu et al. (2010), who accidentally used a smaller Greenland land mask function. Their revised estimate with the new land-sea mask yields 160 ± 16 GT·a⁻¹ mass loss (Wu et al., 2011). Despite the large inter-annual variability in mass loss rate as shown in Shepherd et al. (2020), our Greenland estimate agrees well with the latest IMBIE Greenland result. Based on the IMBIE data sets, the average Greenland ice sheet mass change rate is 199 GT·a⁻¹ from 2002.0 to 2010.0. We include a handful of GPS sites in Greenland that were installed after 2007, these sites are recording faster melting rate between 2007 and 2010 that can lead to slightly increased overall melting rate in Greenland. Our new estimate in Greenland is smaller than recent GRACE based results because our high-resolution inversion is able to separate mass losses in Greenland proper from those over its peripheral areas. Mass redistribution due to glacier melting has been found in the Canadian Arctic Archipelago, Iceland, Svalbard, the Arctic Ocean, and SE Alaska, the Antarctic Peninsula, Patagonia, and high mountain glacier regions in Asia. We report an average of 5.6 ± 16.7 GT·a⁻¹ mass change rate in East Antarctica

over the period of 2002–2010, statistically indistinguishable from zero. Our results reconcile with other results in East Antarctica averaged over the past two decades (Shepherd et al., 2018). However, we recall the large inter-annual variability in surface mass balance in Antarctica, and therefore, comparing results of different periods may lead to incorrect conclusions. Although the coseismic deformation patterns for the two largest earthquakes during the study period are removed from the geoid change rate, a residual pattern can be seen in this region possibly due to slightly different post-seismic deformation patterns. But such aliasing effects are very much localized and will not impact our global results. We find a general pattern of mass increase in the US high plains and the Prairies in Canada, likely caused by an increased precipitation. The patterns are significant, because the uncertainties for PDMT are generally an order of magnitude smaller than the PDMT values themselves. The largest uncertainty is located in the interior of Antarctica, due to a lack of land-based GPS data.

Our method provides a robust estimation of global GIA and its uncertainty. Although our GIA estimate is different from other global GIA models as it also includes the effect from recent ice mass changes, it recovers the large-scale global GIA pattern in recent models, while differs considerably in some regions (Figure 5). The most striking difference is the uplift found in West Antarctica, near the Amundsen Sea Embayment (ASE). The uplift center near the ASE is suggested to be due to the fast mantle viscous response to recent ice melting (Nielsen et al., 2014). Recent seismic tomography studies reveal drastically different S wave velocity contrast for East and West Antarctica, with the latter inferred to have an

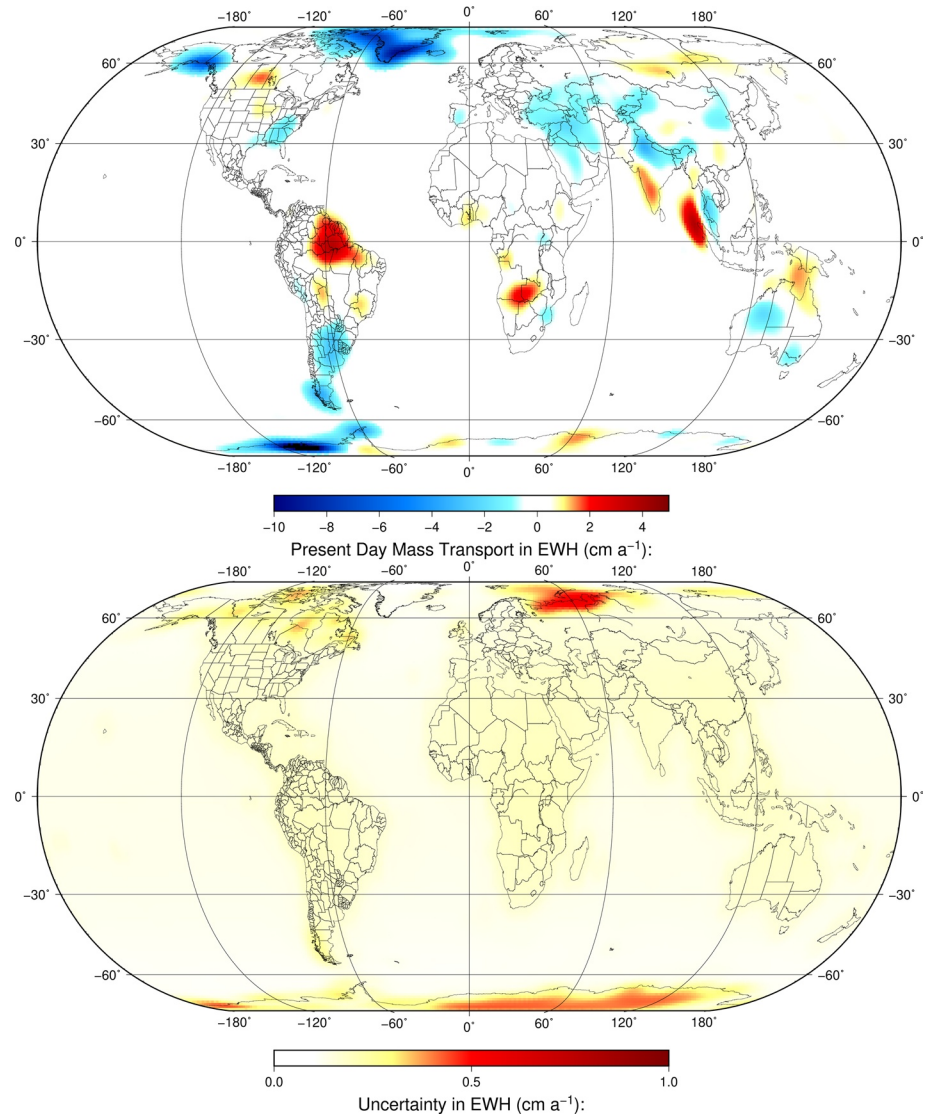


Figure 4. Global distribution of PDMT from 2002 to 2010 from the global inversion, expressed in EWH in $\text{cm}\cdot\text{a}^{-1}$. A 350-km Gaussian filter is applied to the PDMT spherical harmonic coefficients to smooth the result. The lower panel shows the uncertainty associated with the PDMT estimates, expressed in EWH. Note that most areas have uncertainties less than $0.5 \text{ cm}\cdot\text{a}^{-1}$. EWH, equivalent water height; PDMT, present-day mass transport.

anomalously high upper mantle temperature and a thin lithosphere (An et al., 2015). This combination of high mantle temperature and thin lithosphere likely leads to the fast visco-elastic response to the melting in the recent past, which induces regional uplift rates of more than $20 \text{ mm}\cdot\text{a}^{-1}$ near ASE. Few GIA models consider lateral heterogeneity in the Earth structure (van der Wal et al., 2015) and recent ice melting (Nield et al., 2014), making a direct comparison of GIA models with our results difficult in areas similar to ASE. Our inversion shows enhanced viscous response in areas of low effective viscosity, thin asthenosphere and rapid melting in the recent past, such as Southeast Alaska, the west coast of Canada, Iceland, Svalbard, and the Antarctica Peninsula. Global GIA models built on data from other regions, and data from before the ice change in the last centuries (e.g., RSL data) generally do not show enhanced viscous response of GIA, and can introduce errors if used to correct observations for present-day ice mass change estimates.

We separate large-scale PDMT and GIA-induced deformation and geoid changes by conducting an inversion in the spectral domain with a global distribution of multiple observation types (Table 1). Our results

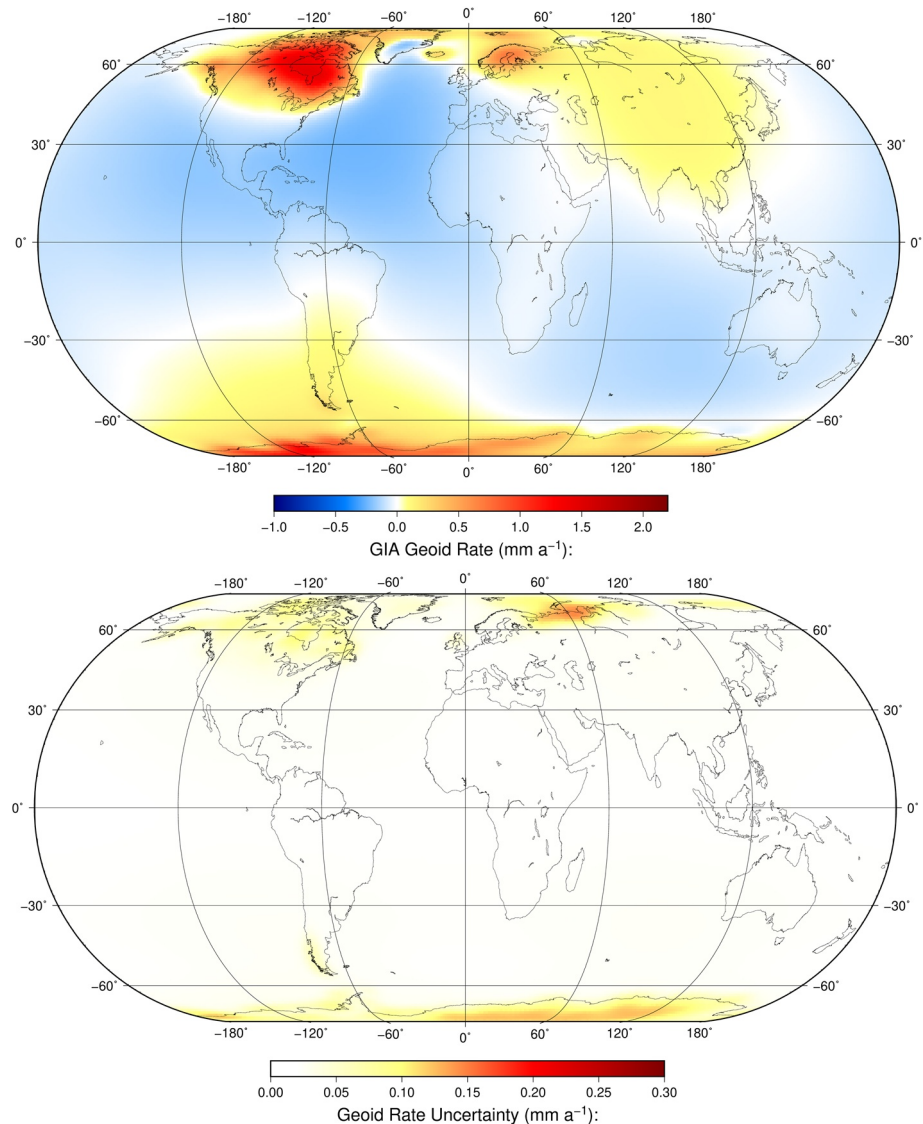


Figure 5. Estimated GIA geoid rate and its uncertainty from the global inversion. Upper figure shows GIA induced geoid change rate, with positive anomaly in red and negative anomaly in blue. We also calculated uncertainty of the GIA geoid, which is roughly one order of magnitude smaller than the GIA geoid rate. The two regions of larger uncertainty are found in Far North Russia and East Antarctica, presumably related to the lack of land geodetic stations to separate GIA from PDMT. GIA, glacial isostatic adjustment; OBP, ocean bottom pressure; PDMT, present-day surface mass trend.

show a GIA-induced \dot{J}_2 similar to the one found by Wu et al. (2010). It is also very close to the SLR total \dot{J}_2 observation before the early 1990s (Roy & Peltier, 2011). PDMT \dot{J}_2 shows a large positive value owing to the increased Earth oblateness from polar ice melting since the 1990s (Roy & Peltier, 2011). Our determined PDMT geocenter motion is small, with $-0.16 \pm 0.08 \text{ mm}\cdot\text{a}^{-1}$ along the Z-axis, contributing about $15 \text{ GT}\cdot\text{a}^{-1}$ to mass change in Antarctica. The values of the separate components differ from those in Wu et al. (2010), most likely due to the increased a priori uncertainties in long-wavelength OBP rates and thus their reduced weights in the inversion. The GIA-induced geocenter motion estimate remains very similar to that of Wu et al. (2010), which is significantly larger in magnitude than -0.4 to $-0.5 \text{ mm}\cdot\text{a}^{-1}$ indicated by traditional GIA models and much larger than that induced by PDMT.

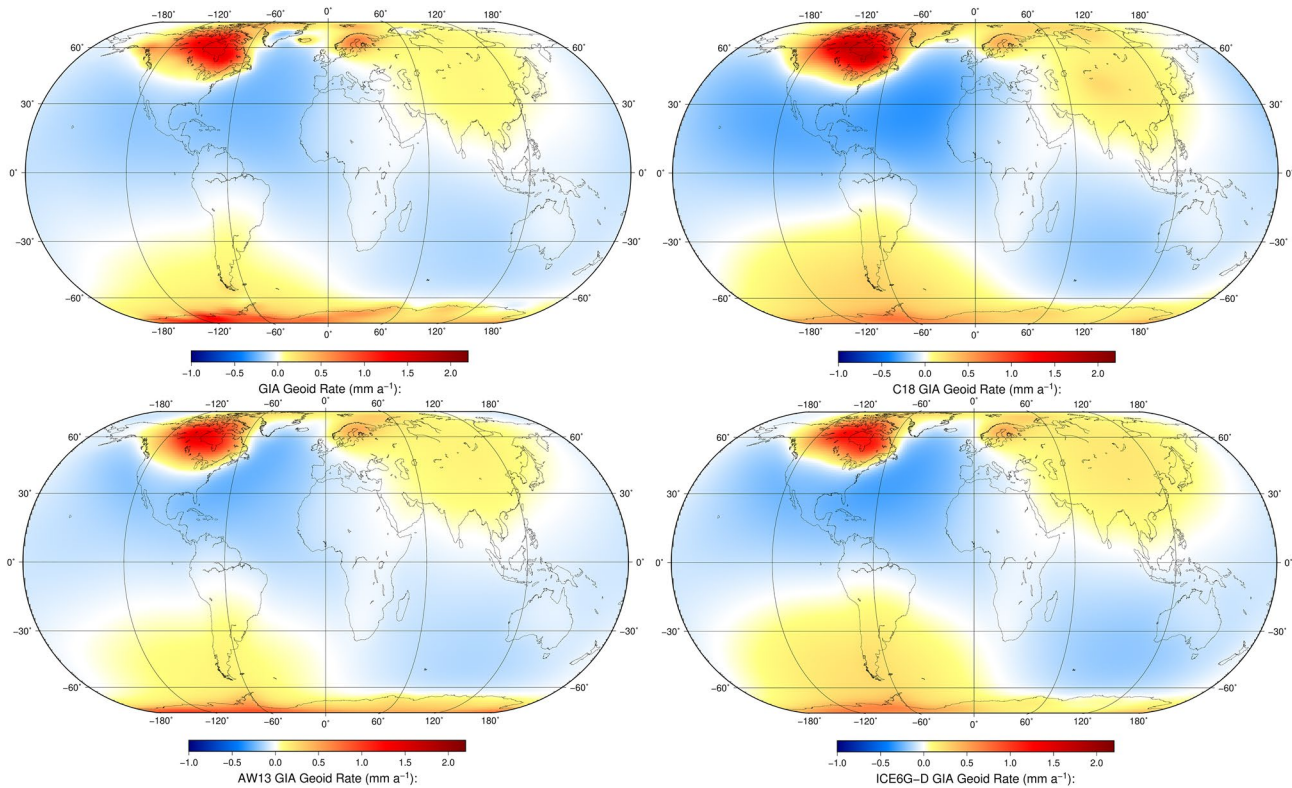


Figure 6. Comparison of global GIA geoid rate estimates. We compare our inverted GIA geoid rate with three model results, C18 (Caron et al., 2018), AW13 (A et al., 2013), and ICE6G-D (Peltier et al., 2018). All three geoid rates have been smoothed with a 300 km Gaussian filter and are downloaded from JPL's PODAAC data center (Last accessed, 2020-04-25).

5. Discussions and Conclusions

Although advances have been made in GIA modeling during the past decades, for example, Peltier et al. (2018) and quantification of GIA model uncertainty (Caron et al., 2018; Li et al., 2020), large discrepancies remain in different GIA models and model-based GIA corrections to PDMT (Shepherd et al., 2018). Further, errors in GIA models are difficult to quantify because most are built based on a forward-fitting approach or partial domain inverse that suffers from non-uniqueness in the obtained earth and ice history parameters (e.g., Paulson et al., 2007b) and limited coverage of GIA observations which can bias the predictions in data-sparse regions. Subsequent iterative modifications have also been carried out to adjust the load and rheology parameters to forward-fit additional data. Also, most GIA models use a spherically symmetric Earth structure, which ignores the impact of lateral homogeneity. More advanced numerical models with realistic rheology are computationally expensive, and require more detailed observations of Earth composition. Our inversion benefits from relatively dense globally distributed observation networks. By exploiting intrinsic relations among gravity and deformation due to PDMT and GIA, we separate their signatures and provide realistic uncertainty estimates. A spherically symmetric Earth structure is used and only a few depth-dependent rheological parameters are perturbed in the construction of the a priori GIA covariance matrix. However, very heterogeneous ice history and large mantle viscosity uncertainties are allowed. Given the ambiguities between ice history and Earth rheology in interpreting modern geodetic data, possible lateral heterogeneity in Earth rheology should not have a significant impact on our kinematic inversion, because geodetic GIA signatures due to lower upper mantle viscosity may be compensated by indiscernible signatures due to stronger melting, and vice versa.

Rapid visco-elastic response to deglaciation in the recent past in areas of low upper mantle viscosity and thin crust is also suggested by our results. Most affected zones are near subduction zones (e.g., Western Canada and SE Alaska; Patagonia) or close to known weak mantle zones (e.g., Iceland, ASE). Inferred upper

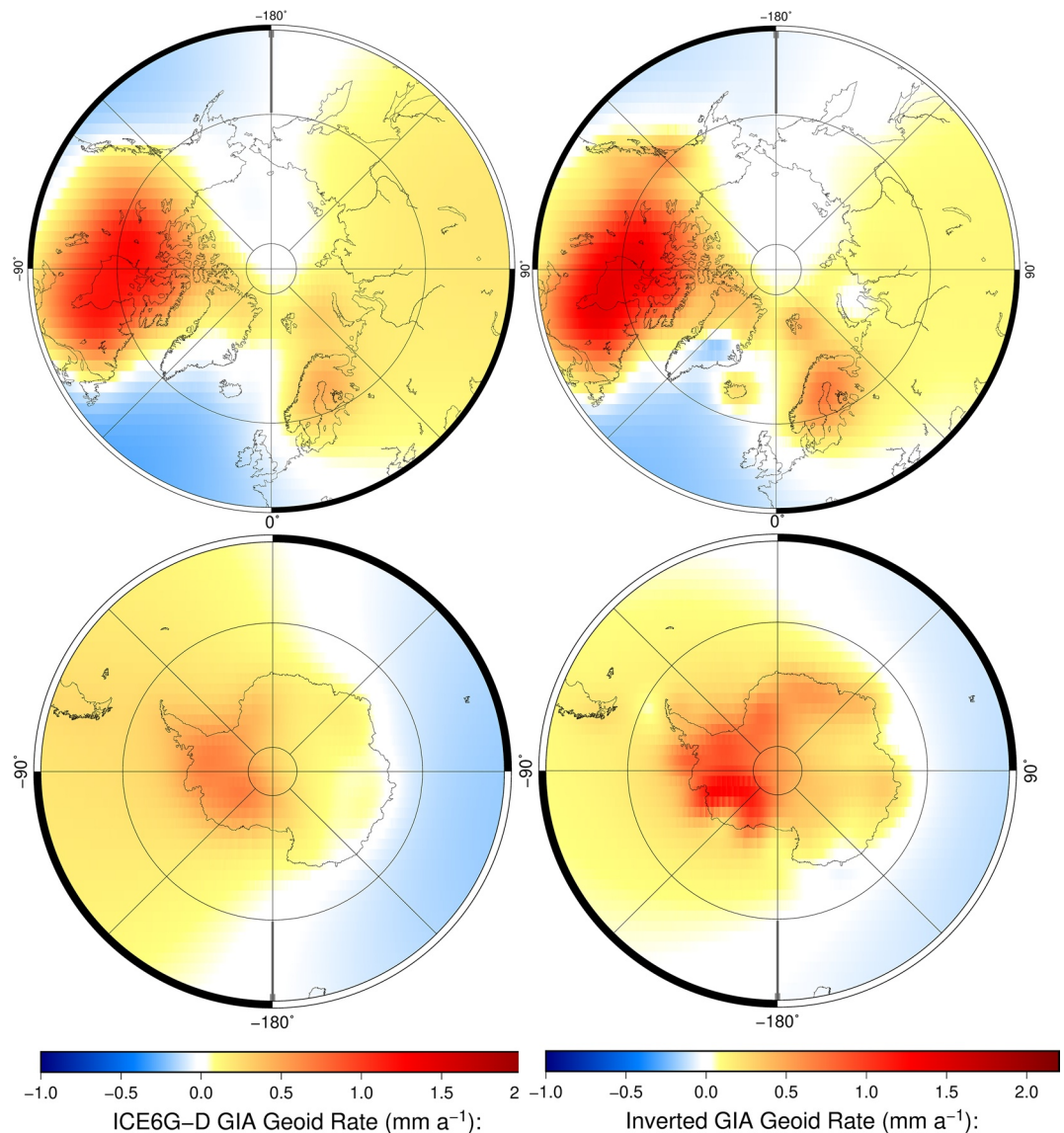


Figure 7. Comparison of GIA geoid rate in the polar regions. The left panel are plots of the ICE6G-D (Peltier et al., 2018) geoid rate in the North and South Pole. The right are two plots of our GIA inversion results in the same region. GIA, glacial isostatic adjustment.

mantle viscosity from seismological and geodetic data in those regions are near 10^{18} Pa-s (James et al., 2009; Larsen et al., 2005), two orders of magnitude lower than the global average value. This brings the load-induced solid earth response time down to 10^1 – 10^2 years. Our result validates those regional models, and on top of that provides estimates of low-degree spherical harmonic coefficients that can improve the accuracy of our regional estimates and hence the accuracy of mass balance estimates obtained from joint inversion. We compare our global present-day GIA geoid rate with three other dynamically constructed GIA models (Figure 6). Even though our a priori GIA model differs from more recent GIA models, the long-wavelength pattern of these models (Caron et al., 2018; A et al., 2013; Peltier et al., 2018) is recovered well, which could indicate that effects of lateral heterogeneity that is allowed in our inversion are relatively small. Our GIA J_2 is very close to that of ICE-6G and pre-1992 SLR observations (Roy & Peltier, 2011), although our inverted GIA geoid includes the effect of enhanced GIA. This indicates a small effect of 3D Earth structure to global scale deformation or this effect is balanced by a slightly different values of mantle viscosity. In addition, we find our result showing enhanced GIA viscoelastic responses in areas with possible recent past ice mass changes. In the Polar Region, our GIA geoid shows enhanced positive geoid rates in SE Alaska and West-

ern Canada, Iceland, Svalbard, ASE, and in the coastal areas of East Antarctica (Figure 7). We also find a negative geoid rate in southeast Greenland that is less clear in other models. This negative anomaly does not affect the accuracy of PDMT estimates in Greenland as our result agrees well with the latest IMBIE estimates in Greenland. We compare our GIA results and ICE-6G in Greenland and find the absolute difference between them is less than $0.2 \text{ mm}\cdot\text{a}^{-1}$. Such a difference is possible from variations in 3D Earth structures (e.g., Milne et al., 2018). We speculate this signal could be real geophysical signal, for example, influence of the lateral heterogeneous Earth structure (Milne et al., 2018), past ice mass fluctuations, or a combination of both. Because GIA induced bedrock uplift serves to reduce the water depth near the marine based ice sheet, it acts to slow down the rate of ice loss (Gomez et al., 2010). In regions of low mantle viscosity (e.g., ASE), the stabilizing effect will be stronger. Our result can provide better estimates of current vertical rate in those regions, and contribute to better modeling of the coupled effect of tectonic and ice dynamics in marine based ice sheets. Furthermore, using an ice history that includes late Holocene ice mass change and accounting for Earth's lateral structural heterogeneity will improve estimates of present-day GIA signatures on both local and global scales for the forward models.

Till date, most data-driven GIA models developed are used to understand regional GIA or PDMT signals (Gunter et al., 2014; Martín-Español et al., 2016; Sasgen et al., 2017; Simon et al., 2017). By including multiple global data sets, our simultaneous global inversion separates long-wavelength PDMT and GIA signatures and avoids the related biases in the regional approaches. On the other hand, since our method is conducted in the spectral domain, the small scale results may be perturbed by the truncation error. We improve the accuracy of our method by including a high-resolution land-sea mask, incorporating a physically plausible a priori information, and a modified SVD solver to solve the least square problem. The low-degree GIA spherical harmonic coefficients offer insights into deep Earth rheology and global change history. Our results confirm that GIA-induced geocenter velocity is larger than the standard model predictions (Wu et al., 2010), but GIA-induced \dot{J}_2 is consistent with the model value adopted from earlier SLR observations (Peltier, 2004) and in stark contrast with the $-(6.0-6.5) \times 10^{-11} \text{ a}^{-1}$ value based on the SLR/AR5 scenario (Nakada et al., 2015).

Although it is not a dynamic inversion for earth rheology and ice history, our unique approach provides a robust separation of GIA signatures from those of PDMT. We provide a snapshot view of GIA and PDMT at present-day with realistic estimations of uncertainties. The derived GIA rates, along with their uncertainties, can be used to reveal weakness in the data sets and chart for future improvements. Our method has the potential to include more observations, such as paleo relative sea level (RSL) data to conduct a global inversion with PDMT and dynamic GIA parameters. Current ice history models are largely built by forward-fitting the RSL records without a quantitative uncertainty assessment. This unfortunate situation led to the very conservative a priori GIA information which has to discard a large amount of information contained in the global RSL records. A dynamic global inversion incorporating RSL data will not only remedy this problem, but also gain insights into deep earth rheology, reconcile the difference in mantle viscosity from geodetic and seismic data, and further constrain ice history, in an unambiguous way.

The causes and the validity of the ICB are still under debate (Borsa et al., 2019). Given the relatively small ice sheet surface extent, the impact of the ICB on Greenland mass balance estimation is relatively small. However, owing to the large extent of the Antarctic ice sheet, $1 \text{ cm}\cdot\text{a}^{-1}$ of ice elevation change in Antarctica roughly translates to $100 \text{ GT}\cdot\text{a}^{-1}$ mass change. This implies that the accuracy of ICESat ICB estimates is critical when evaluating Antarctic ice mass balance. Conventionally, the ICBs are validated/calibrated with independent in situ measurements over time (Borsa, et al., 2019; Schröder, et al., 2017; Zwally et al., 2015). In this study, we take advantage of the globally distributed data sets to estimate the ICB trend directly from data. We use RL634 GLA12 data products (Antarctica and Greenland Ice Sheet Altimetry Data). It is reasonable to assume a constant ICB trend for ICESat measurement over the ice sheets in Greenland and Antarctica. We parameterize the ICB trend into our inverse formulization. Although our parameterization method does not determine ICBs on individual laser campaigns, the trend estimation has a small uncertainty, probably reflects the improved statistics from stacking a large amount of data. Our ICB trend agrees well with the latest result of Schröder et al. (2017), who estimated the ICB trend (L2a-L2d) to be $6.8 \pm 4.1 \text{ mm}\cdot\text{a}^{-1}$, although we notice a large increase of the ICB trend in their reported result if the last two laser campaigns are included. The amount of data from the last two ICESat laser campaigns are rela-

tively small, and will have very limited overall impact on our estimated trend. For the same period, Borsa et al. (2019) determines the ICB trend to be $2 \pm 4 \text{ mm}\cdot\text{a}^{-1}$, suggesting a statistically insignificant ICB trend in their study area (The salar de Uyuni, Bolivia). One source of the spatially varying ICB trends is the switch of ITRF reference frames during the course of the ICESat mission. The ICESat elevations were geolocated to the ITRF2000 (on and before November 5, 2006) and ITRF2005 (on and after November 6, 2006) separately (Urban et al., 2011). This complication in reference frame introduces a $-5.8 \pm 0.3 \text{ mm}$ translation and a $-1.8 \pm 0.3 \text{ mm}\cdot\text{a}^{-1}$ translation rate in the Z axis start on the epoch of 2000.0. This origin drift in the Z -axis will have limited impact on height change in the tropical area, and mostly will manifest itself as horizontal deformation. But most of it will translate into height change in Antarctica. Since none of the studies correct for this frame change, it will introduce a cumulative subsidence of 2–3 cm for ICESat derived products (campaign L2g-L2d) in Antarctica and 1–2 cm uplift in Greenland. Although we did not consider the effect of frame translation in ICESat height rate as its overall effect will be corrected by the additional ICB trend parameter. It is advised that future studies utilizing the ICESat data should correct the bias introduced by switching the ITRF frames.

In this paper, we present results from a mostly data-driven global inversion method that provides estimates of PDMT and kinematic GIA signatures with their uncertainties. The PDMT and GIA results are only weakly dependent on the a priori GIA model, and can be used to validate the dynamically constructed forward model, or to provide GIA corrections to the GRACE-FO mission. Our results show enhanced GIA signals in the regions of low mantle viscosity and recent deglaciation that are consistent with regional studies, but which were not present in global GIA model results. We provide new estimates of low-degree GIA spherical harmonic coefficients that are related to deep earth rheology. Our results confirm the earlier GIA J_2 estimation from SLR data. The estimated ICESat inter-campaign bias trend is similar to the most recent study using in situ data in Antarctica.

Data Availability Statement

ICESat data are available at the NASA distributed active archive center (<https://nsidc.org/data/icesat/data.html>). GRACE level 2 data were obtained from the NASA Physical Oceanography Distributed Active Archive Center (PO.DAAC, <https://podaac.jpl.nasa.gov/GRACE>). GPS data were obtained from the UNAVCO (<ftp://data-out.unavco.org/pub/rinex/obs/>) and the IGS data center (<https://cddis.nasa.gov/archive/gnss/data/daily>), and from the Canadian Geodetic Survey (<https://www.nrcan.gc.ca/maps-tools-publications/maps/data/10923>). ECCO data are available at the NASA PO.DAAC data center (<https://ecco-group.org/products.htm>). This is GSC contribution 2019003039.

References

- A, G., Wahr, J., & Zhong, S. (2013). Computations of the viscoelastic response of a 3-D compressible Earth to surface loading: An application to Glacial Isostatic Adjustment in Antarctica and Canada. *Geophysical Journal International*, 192(2), 557–572. <https://doi.org/10.1093/gji/ggs030>
- An, M., Wiens, D. A., Zhao, Y., Feng, M., Nyblade, A., Kanao, M., et al. (2015). Temperature, lithosphere-asthenosphere boundary, and heat flux beneath the Antarctic Plate inferred from seismic velocities. *Journal of Geophysical Research: Solid Earth*, 120(12), 8720–8742. <https://doi.org/10.1002/2015jb011917>
- Blewitt, G., Lavallée, D., Clarke, P., & Nurutdinov, K. (2001). A new global mode of Earth deformation: Seasonal cycle detected. *Science*, 294(5550), 2342–2345. <https://doi.org/10.1126/science.1065328>
- Boehm, J., Werl, B., & Schuh, H. (2006). Troposphere mapping functions for GPS and very long baseline interferometry from European Centre for Medium-Range Weather Forecasts operational analysis data. *Journal of Geophysical Research*, 111(B2). <https://doi.org/10.1029/2005jb003629>
- Borsa, A. A., Fricker, H. A., & Brunt, K. M. (2019). A terrestrial validation of ICESat elevation measurements and implications for global reanalyses. *IEEE Transactions on Geoscience and Remote Sensing*, 57(9), 6946–6959. <https://doi.org/10.1109/tgrs.2019.2909739>
- Borsa, A. A., Moholdt, G., Fricker, H. A., & Brunt, K. M. (2014). A range correction for ICESat and its potential impact on ice-sheet mass balance studies. *The Cryosphere*, 8(2), 345–357. <https://doi.org/10.5194/tc-8-345-2014>
- Caron, L., & Ivins, E. R. (2020). A baseline Antarctic GIA correction for space gravimetry. *Earth and Planetary Science Letters*, 531, 115957. <https://doi.org/10.1016/j.epsl.2019.115957>
- Caron, L., Ivins, E. R., Larour, E., Adhikari, S., Nilsson, J., & Blewitt, G. (2018). GIA model statistics for GRACE hydrology, cryosphere, and ocean science. *Geophysical Research Letters*, 45(5), 2203–2212. <https://doi.org/10.1002/2017gl076644>
- Cheng, M., Tapley, B. D., & Ries, J. C. (2013). Deceleration in the Earth's oblateness. *Journal of Geophysical Research: Solid Earth*, 118(2), 740–747. <https://doi.org/10.1002/jgrb.50058>
- Cox, C. M., & Chao, B. F. (2002). Detection of a large-scale mass redistribution in the terrestrial system since 1998. *Science*, 297(5582), 831–833. <https://doi.org/10.1126/science.1072188>

Acknowledgments

This work was supported by the NASA Earth Surface and Interior Program (grant number 16-ESI16-0009) and Natural Resources Canada's climate change and adaptation program. The research was partially carried out at the Jet Propulsion Laboratory, California Institute of Technology, under a contract with the National Aeronautics and Space Administration (NASA). The authors acknowledge the partial US government sponsorship by the NASA'S GRACE Science Team and Earth Surface and Interior programs. The authors are grateful to the operators of ICESat, GPS, GRACE, and ECCO data archive for providing access to the data used in this study. Comments from two anonymous reviewers helped to improve this manuscript.

- DeMets, C., Gordon, R. G., & Argus, D. F. (2010). Geologically current plate motions. *Geophysical Journal International*, 181(1), 1–80. <https://doi.org/10.1111/j.1365-246x.2009.04491.x>
- Dickey, J. O., Marcus, S. L., de Viron, O., & Fukumori, I. (2002). Recent earth oblateness variations: Unraveling climate and postglacial rebound effects. *Science*, 298(5600), 1975–1977. <https://doi.org/10.1126/science.1077777>
- Dobslaw, H., & Thomas, M. (2007). Simulation and observation of global ocean mass anomalies. *Journal of Geophysical Research*, 112(C5). <https://doi.org/10.1029/2006jc004035>
- Farrell, W. E. (1972). Deformation of the Earth by surface loads. *Reviews of Geophysics*, 10(3), 761–797. <https://doi.org/10.1029/RG010i003p00761>
- Fukumori, I., Raghunath, R., Fu, L.-L., & Chao, Y. (1999). Assimilation of TOPEX/Poseidon altimeter data into a global ocean circulation model: How good are the results? *Journal of Geophysical Research*, 104(C11), 25647–25665. <https://doi.org/10.1029/1999jc900193>
- Gomez, N., Mitrovica, J. X., Huybers, P., & Clark, P. U. (2010). Sea level as a stabilizing factor for marine-ice-sheet grounding lines. *Nature Geoscience*, 3, 850–853. <https://doi.org/10.1038/ngeo1012>
- Gunter, B. C., Didova, O., Riva, R. E. M., Ligtenberg, S. R. M., Lenaerts, J. T. M., King, M. A., et al. (2014). Empirical estimation of present-day Antarctic glacial isostatic adjustment and ice mass change. *The Cryosphere*, 8, 743–760. <https://doi.org/10.5194/tc-8-743-2014>
- Han, S.-C., Riva, R., Sauber, J., & Okal, E. (2013). Source parameter inversion for recent great earthquakes from a decade-long observation of global gravity fields. *Journal of Geophysical Research: Solid Earth*, 118, 1240–1267. <https://doi.org/10.1002/jgrb.50116>
- Harig, C., & Simons, F. J. (2015). Accelerated West Antarctic ice mass loss continues to outpace East Antarctic gains. *Earth and Planetary Science Letters*, 415, 134–141. <https://doi.org/10.1016/j.epsl.2015.01.029>
- Ivins, E. R., & James, T. S. (2005). Antarctic glacial isostatic adjustment: A new assessment. *Antarctic science*, 17(4), 541–553. <https://doi.org/10.1017/S0954102005002968>
- Ivins, E. R., James, T. S., Wahr, J., Schrama, E. J. O., Simon, K. M., & Simon, K. M. (2013). Antarctic contribution to sea level rise observed by GRACE with improved GIA correction. *Journal of Geophysical Research: Solid Earth*, 118(6), 3126–3141. <https://doi.org/10.1002/jgrb.50208>
- Jacob, T., Wahr, J., Pfeffer, W. T., & Swenson, S. (2012). Recent contributions of glaciers and ice caps to sea level rise. *Nature*, 482, 514–518. <https://doi.org/10.1038/nature10847>
- James, T. S., Gowan, E. J., Wada, I., & Wang, K. (2009). Viscosity of the asthenosphere from glacial isostatic adjustment and subduction dynamics at the northern Cascadia subduction zone, British Columbia, Canada. *Journal of Geophysical Research*, 114(B4). <https://doi.org/10.1029/2008JB006077>
- Jiang, Y., Dixon, T. H., & Wdowinski, S. (2010). Accelerating uplift in the North Atlantic region as an indicator of ice loss. *Nature Geoscience*, 3(6), 404–407. <https://doi.org/10.1038/ngeo845>
- Jiang, Y., Wdowinski, S., Dixon, T. H., Hackl, M., Protti, M., & Gonzalez, V. (2012). Slow slip events in Costa Rica detected by continuous GPS observations, 2002–2011. *Geochemistry, Geophysics, Geosystems*, 13(4). <https://doi.org/10.1029/2012gc004058>
- Larsen, C. F., Motyka, R. J., Freymueller, J. T., Echelmeyer, K. A., & Ivins, E. R. (2005). Rapid viscoelastic uplift in southeast Alaska caused by post-Little Ice Age glacial retreat. *Earth and Planetary Science Letters*, 237(3), 548–560. <https://doi.org/10.1016/j.epsl.2005.06.032>
- Li, T., Wu, P., Wang, H., Steffen, H., Khan, N. S., Engelhart, S. E., et al. (2020). Uncertainties of glacial isostatic adjustment model predictions in North America associated with 3D structure. *Geophysical Research Letters*, 47, e2020GL087944. <https://doi.org/10.1029/2020gl087944>
- Lucas-Picher, P., Wulff-Nielsen, M., Christensen, J. H., Aðalgeirsdóttir, G., Mottram, R., & Simonsen, S. B. (2012). Very high resolution regional climate model simulations over Greenland: Identifying added value. *Journal of Geophysical Research*, 117(D2). <https://doi.org/10.1029/2011jd016267>
- Lyard, F., Lefevre, F., Letellier, T., & Francis, O. (2006). Modelling the global ocean tides: Modern insights from FES2004. *Ocean Dynamics*, 56(5), 394–415. <https://doi.org/10.1007/s10236-006-0086-x>
- Martin-Español, A., Zammit-Mangion, A., Clarke, P. J., Flament, T., Helm, V., King, M. A., et al. (2016). Spatial and temporal Antarctic Ice Sheet mass trends, glacio-isostatic adjustment, and surface processes from a joint inversion of satellite altimeter, gravity, and GPS data. *Journal of Geophysical Research: Earth Surface*, 121(2), 182–200. <https://doi.org/10.1002/2015jef003550>
- Milne, G. A., Latychev, K., Schaeffer, A., Crowley, J. W., Lecavalier, B. S., & Audette, A. (2018). The influence of lateral Earth structure on glacial isostatic adjustment in Greenland. *Geophysical Journal International*, 214(2), 1252–1266. <https://doi.org/10.1093/gji/ggy189>
- Mitrovica, J. X., Wahr, J., Matsuyama, I., & Paulson, A. (2005). The rotational stability of an ice-age earth. *Geophysical Journal International*, 161(2), 491–506. <https://doi.org/10.1111/j.1365-246x.2005.02609.x>
- Nakada, M., Okuno, J. i., Lambeck, K., & Purcell, A. (2015). Viscosity structure of Earth's mantle inferred from rotational variations due to GIA process and recent melting events. *Geophysical Journal International*, 202(2), 976–992. <https://doi.org/10.1093/gji/ggv198>
- Nield, G. A., Barletta, V. R., Bordoni, A., King, M. A., Whitehouse, P. L., Clarke, P. J., et al. (2014). Rapid bedrock uplift in the Antarctic Peninsula explained by viscoelastic response to recent ice unloading. *Earth and Planetary Science Letters*, 397, 32–41. <https://doi.org/10.1016/j.epsl.2014.04.019>
- Paulson, A., Zhong, S., & Wahr, J. (2007a). Inference of mantle viscosity from GRACE and relative sea level data. *Journal of Intelligence*, 171, 497–508. <https://doi.org/10.1111/j.1365-246x.2007.03556.x>
- Paulson, A., Zhong, S., & Wahr, J. (2007b). Limitations on the inversion for mantle viscosity from postglacial rebound. *Geophysical Journal International*, 168(3), 1195–1209. <https://doi.org/10.1111/j.1365-246x.2006.03222.x>
- Peltier, W. R. (2004). Global glacial isostasy and the surface of the ice-age Earth: The ICE-5G (VM2) model and GRACE. *Annual Review of Earth and Planetary Sciences*, 32(1), 111–149. <https://doi.org/10.1146/annurev.earth.32.082503.144359>
- Peltier, W. R. (2015). The history of the Earth's rotation: Impacts of deep earth physics and surface climate variability. In G. Schubert (Ed.), *The treatise on geophysics* (2nd ed., pp 221–279). Elsevier. <https://doi.org/10.1016/b978-0-444-53802-4.00161-5>
- Peltier, W. R., Argus, D. F., & Drummond, R. (2015). Space geodesy constrains ice age terminal deglaciation: The global ICE-6G_C (VM5a) model. *Journal of Geophysical Research: Solid Earth*, 120(1), 450–487. <https://doi.org/10.1002/2014jb011176>
- Peltier, W. R., Argus, D. F., & Drummond, R. (2018). Comment on “An assessment of the ICE-6G_C (VM5a) glacial isostatic adjustment model” by Purcell et al. *Journal of Geophysical Research: Solid Earth*, 123, 2019–2028. <https://doi.org/10.1002/2016JB013844>
- Rebschung, P., Griffiths, J., Ray, J., Schmid, R., Collilieux, X., & Garayt, B. (2012). IGS08: The IGS realization of ITRF2008. *GPS Solutions*, 16(4), 483–494. <https://doi.org/10.1007/s10291-011-0248-2>
- Roy, K., & Peltier, W. R. (2011). GRACE era secular trends in Earth rotation parameters: A global scale impact of the global warming process? *Geophysical Research Letters*, 38, L10306. <https://doi.org/10.1029/2011GL047282>
- Sasgen, I., Martín-Español, A., Horvath, A., Klemann, V., Petrie, E. J., Wouters, B., et al. (2017). Joint inversion estimate of regional glacial isostatic adjustment in Antarctica considering a lateral varying Earth structure (ESA STSE Project REGINA). *Geophysical Journal International*, 211(3), 1534–1553. <https://doi.org/10.1093/gji/ggx368>

- Scambos, T., & Shuman, C. (2016). Comment on 'Mass gains of the Antarctic ice sheet exceed losses' by H. J. Zwally and others. *Journal of Glaciology*, 62(233), 599–603. <https://doi.org/10.1017/jog.2016.59>
- Scambos, T. A., Bohlander, J. A., Shuman, C. A., & Skvarca, P. (2004). Glacier acceleration and thinning after ice shelf collapse in the Larsen B embayment, Antarctica. *Geophysical Research Letters*, 31(18). <https://doi.org/10.1029/2004gl020670>
- Schröder, L., Richter, A. J., Fedorov, D. V., Eberlein, L., Brovko, E. V., Popov, S. V., et al. (2017). Validation of satellite altimetry by kinematic GNSS in central East Antarctica.
- Schutz, B. E., Zwally, H. J., Shuman, C. A., Hancock, D., & DiMarzio, J. P. (2005). Overview of the ICESat Mission. *Geophysical Research Letters*, 32(21). <https://doi.org/10.1029/2005gl024009>
- Shepherd, A., Ivins, E., Rignot, E., Smith, B., van den Broeke, M., Velicogna, I., et al. (2018). Mass balance of the Antarctic Ice Sheet from 1992 to 2017. *Nature*, 558(7709), 219–222. <https://doi.org/10.1038/s41586-018-0179-y>
- Shepherd, A., Ivins, E., Rignot, E., Smith, B., van den Broeke, M., Velicogna, I., et al. (2020). Mass balance of the Greenland Ice Sheet from 1992 to 2018. *Nature*, 579, 233–239. <https://doi.org/10.1038/s41586-019-1855-2>
- Simon, K. M., Riva, R. E. M., Kleinerherenbrink, M., & Tangdamrongsub, N. (2017). A data-driven model for constraint of present-day glacial isostatic adjustment in North America. *Earth and Planetary Science Letters*, 474, 322–333. <https://doi.org/10.1016/j.epsl.2017.06.046>
- Simonsen, S. B., Stenseng, L., Adalgeirsdóttir, G., Fausto, R. S., Hvidberg, C. S., & Lucas-Picher, P. (2013). Assessing a multilayered dynamic firn-compaction model for Greenland with ASIRAS radar measurements. *Journal of Glaciology*, 59(215), 545–558. <https://doi.org/10.3189/2013JoG12J158>
- Sørensen, L. S., Simonsen, S. B., Nielsen, K., Lucas-Picher, P., Spada, G., Adalgeirsdóttir, G., et al. (2011). Mass balance of the Greenland ice sheet (2003–2008) from ICESat data - the impact of interpolation, sampling and firn density. *The Cryosphere*, 5(1), 173–186. <https://doi.org/10.5194/tc-5-173-2011>
- Tapley, B. D., Bettadpur, S., Ries, J. C., Thompson, P. F., & Watkins, M. M. (2004). GRACE measurements of mass variability in the Earth system. *Science*, 305(5683), 503–505. <https://doi.org/10.1126/science.1099192>
- Tushingham, A. M., & Peltier, W. R. (1991). Ice-3G: A new global model of Late Pleistocene deglaciation based upon geophysical predictions of post-glacial relative sea level change. *Journal of Geophysical Research*, 96, 4497–4523. <https://doi.org/10.1029/90jb01583>
- Urban, T., Bae, S., Rim, H.-J., Webb, C., Yoon, S., & Schutz, B. (2011). CSR SCF release notes for orbit and attitude determination, from ICESat/GLAS data, description of data releases. National Snow and Ice Data Center. Retrieved from https://nsidc.org/data/icesat/data_releases.html
- van der Wal, W., Whitehouse, P. L., & Schrama, E. J. O. (2015). Effect of GIA models with 3D composite mantle viscosity on GRACE mass balance estimates for Antarctica. *Earth and Planetary Science Letters*, 414, 134–143. <https://doi.org/10.1016/j.epsl.2015.01.001>
- van Wessem, J. M., van de Berg, W. J., Noël, B. P. Y., van Meijgaard, E., Amory, C., Birnbaum, G., et al. (2018). Modelling the climate and surface mass balance of polar ice sheets using RACMO2 - Part 2: Antarctica (1979–2016). *The Cryosphere*, 12(4), 1479–1498. <https://doi.org/10.5194/tc-12-1479-2018>
- Wahr, J., DaZhong, H., & Trupin, A. (1995). Predictions of vertical uplift caused by changing polar ice volumes on a viscoelastic Earth. *Geophysical Research Letters*, 22(8), 977–980. <https://doi.org/10.1029/94gl02840>
- Wahr, J., Molenaar, M., & Bryan, F. (1998). Time variability of the Earth's gravity field: Hydrological and oceanic effects and their possible detection using GRACE. *Journal of Geophysical Research*, 103(B12), 30205–30229. <https://doi.org/10.1029/98jb02844>
- Wouters, B., Bonin, J. A., Chambers, D. P., Riva, R. E. M., Sasgen, I., & Wahr, J. (2014). GRACE, time-varying gravity, Earth system dynamics and climate change. *Reports on Progress in Physics*, 77(11), 116801. <https://doi.org/10.1088/0034-4885/77/11/116801>
- Wu, X., Collilieux, X., Altamimi, Z., Vermeersen, B., Gross, R., & Fukumori, I. (2011). Inversion of multiple geodetic data sets for geophysical processes and global geodesy. Paper presented at the AGU Fall Meeting Abstracts.
- Wu, X., Heflin, M. B., Schotman, H., Vermeersen, B. L. A., Dong, D., Gross, R. S., et al. (2010). Simultaneous estimation of global present-day water transport and glacial isostatic adjustment. *Nature Geoscience*, 3, 642–646. <https://doi.org/10.1038/ngeo938>. Retrieved from <https://www.nature.com/articles/ngeo938#supplementary-information>
- Zwally, H. J., Li, J., Robbins, J. W., Saba, J. L., Yi, D., & Brenner, A. C. (2015). Mass gains of the Antarctic ice sheet exceed losses. *Journal of Glaciology*, 61(230), 1019–1036. <https://doi.org/10.3189/2015JoG15J071>
- Zwally, H. J., Schutz, B., Abdalati, W., Abshire, J., Bentley, C., Brenner, A., et al. (2002). ICESat's laser measurements of polar ice, atmosphere, ocean, and land. *Journal of Geodynamics*, 34(3), 405–445. [https://doi.org/10.1016/s0264-3707\(02\)00042-x](https://doi.org/10.1016/s0264-3707(02)00042-x)